



Confinement effect of Mn nanoparticles encapsulated in zeolite for efficient catalytic ozonation of S-VOCs at room temperature

Fawei Lin ^a, Luyang Zhang ^a, Hang Du ^c, Yongtao Li ^a, Zhanjun Cheng ^{a,*}, Beibei Yan ^a, Guanyi Chen ^{b,*}

^a School of Environmental Science and Engineering, Tianjin University/Tianjin Key Lab of Biomass/Wastes Utilization, Tianjin 300072, PR China

^b School of Mechanical Engineering, Tianjin University of Commerce, Tianjin 300134, PR China

^c College of Metrology and Measurement Engineering, China Jiliang University, Hangzhou 310018, China



ARTICLE INFO

Keywords:

Catalytic ozonation
Methyl mercaptan
Zeolite
Confinement

ABSTRACT

Catalytic ozonation is potential to eliminate sulfur-containing organic compounds (S-VOCs) with anti-poisoning of sulfur at low temperature. This paper synthesized a popcorn-like catalyst Mn@ZSM293 with confined effect that could combine with ozone to attain 100% conversion of CH₃SH at low temperature, ca. 15 °C, with a low O₃/CH₃SH molar ratio of 1.33. Particularly, excellent stability without sulfur poisoning and good water resistance were observed. By contrast, Mn/ZSM293 exhibited agglomeration of Mn nanoparticles that displayed only 70% conversion at same condition and suffered deactivation. Mn@ZSM293 possessed the structures with well-defined large internal voids and surface etchings, which promoted metal-support interaction. The confined effects also brought more oxygen vacancies, larger surface area and pore size, as well as stronger acidity. These properties were favorable for CH₃SH adsorption, activation and breakage of C–C and C–S bonds. CH₃S[–], CH₃SO₃[–], SO₄^{2–}, and HCOO[–] based compounds were detected as the critical products by in-situ measurement.

1. Introduction

Sulfur-containing organic compounds (S-VOCs) are one of the important potential precursors for photochemical smog and urban haze, which affect physical and mental health of people [1]. Chemical production, landfill, sewage treatment and petroleum refining are the main sources of S-VOC emissions [2]. Chinese government has listed methyl mercaptan, methyl sulfide, dimethyl disulfide and carbon disulfide as the key air pollutants in the emission standards for odorous pollutants. Therefore, development of efficient and stable technology to completely eliminate S-VOCs is of great significance at present. In general, methyl mercaptan (CH₃SH) is usually selected as a typical S-VOCs molecule with high toxicity, corrosivity, and a stench of rotting cabbage, which is also a precursor of some S-VOCs by transformations [3,4].

So far, S-VOCs treatment technology includes combustion, absorption, adsorption and biodegradation, catalytic oxidation, and decomposition [5]. Catalytic directional decomposition of S-VOCs to generate value-added products, such as ethylene, sulfur-containing base materials, and hydrogen sulfide, has potential application prospects [6,7]. Luo's group conducted series of investigation on catalytic

decomposition of S-VOCs [8]. The shorter the carbon chain of mercaptan, the more difficult it is to achieve catalytic degradation. For example, propyl mercaptan (C₃H₇SH) is the easiest for degradation, ethyl mercaptan (C₂H₅SH) is the second one that could reach 100% conversion at 300 °C, while methyl mercaptan (CH₃SH) attained 100% conversion at 400 °C over La-Z5-F catalyst [9]. Besides, catalysts usually suffered poisoning after degradation. They also synthesized Cr/Al₂O₃ catalyst with tuned metal-support interaction that attained 100% conversion of CH₃SH at 375 °C [10]. They also pointed out that the key intermediate promoted the formation of coke and elemental sulfur, leading to covering and/or poisoning of the active sites [11]. Xia et al. [12] further studied the catalytic ozonation of CH₃SH, and found that 0.3% Ag/MnO₂ PHMSs could achieve 95% CH₃SH removal rate, and the addition of Ag enhanced the catalytic effect. He et al. [13] proposed a new process for S-VOCs degradation by wet washing and catalytic ozone oxidation. The elimination rate of CH₃SH by Ag/R-MnO₂ is 96.9%, and the utilization rate of O₃ is 92.3%. Yang et al. [14] tandem catalyzed ozonation of CH₃SH at room temperature. Under the GHSV condition of 60000 mL·h^{–1}·g^{–1}, 5CuO/V₂O₅-MnO₂ can achieve 99% CH₃SH conversion at 25 °C, and the utilization rate of O₃ is 99%. However, sulfur poisoning

* Corresponding authors.

E-mail addresses: zjcheng@tju.edu.cn (Z. Cheng), chengy@tjcu.edu.cn (G. Chen).

is commonly reported to limit its application that sulfate species grabbed the active sites of catalysts preventing the reactants from participating oxidation. S-VOCs elimination techniques include catalytic decomposition, catalytic oxidation and catalytic ozonation. Among them, catalytic decomposition requires high temperature and large energy consumption [15]. While the active substance of catalytic oxidation is only $\cdot\text{OH}$, and there are more sulfur-containing byproducts [16]. Catalytic ozonation is an alternative approach that is potential to attain low temperature degradation of S-VOCs with good stability. Ozone can produce superoxide radicals, i.e., $\cdot\text{OH}$, $\cdot\text{O}_2$, $\cdot\text{O}_2^-$ [17,18], promoting low temperature oxidation. The catalytic ozonation of S is mainly converted to the intermediate product CH_3SO_3 and then further oxidized to SO_4^{2-} . In recent studies, supported precious metals and low-cost metal oxides such as MnO_x , CuO , Co_3O_4 and FeO_x have been developed as effective catalysts for catalytic ozonation of S-VOCs [5,19]. Fenton-like reactions are also applied for S-VOC elimination in water phase with assistance of H_2O_2 over 3D-BiOCl sponge [20]. These researches have validated the feasibility of catalytic ozonation for degradation of S-VOCs and future work should devote to attaining efficient oxidation with low O_3 input and presence of water vapor.

Confined catalyst is expected to solve the above problems due to the characteristics of channel confined effect and interface confined effect [21]. Confined catalysis technology is to design catalysts through two-dimensional interfacial induced structures, channel packaging structures, core-shell structures and defect-derived structures by using interface confined and pore confined effects [22]. Confined structures confine or encapsulate active species in nanometer or subnanometer spaces to provide a unique microenvironment of balanced transition states to regulate chemical reactions [23]. The confined catalysts provide more dispersed active sites through channel and interface limiting, and avoids the aggregation of S species on the surface [16]. Yang et al. prepared zeolite confined bimetallic $\text{PtMn}_{0.2}\text{@ZSM5}$ catalyst for acetone oxidation with a T_{95} of 165 °C [16]. Zhu et al. [24] encapsulated ultra-long $\alpha\text{-MnO}_2$ nanofibers in ultra-thin graphene shells. The 7.50% $\text{MnO}_2\text{@GR}$ catalyst showed a stable ozone conversion efficiency of 80% and excellent stability over 100 h (RH = 20%). Wu et al. [25] prepared $\text{Co}_2\text{Mn}_1\text{O}_8$ core-shell confined catalysts by reversed-phase co-precipitation method, which showed the highest low temperature activity and good thermal stability for catalytic oxidation of C_3H_8 in the presence of 5 vol% H_2O and 5 vol% CO_2 . Conventional nanostructured catalysts are prone to be destructed and poisoned because most of the catalytic active sites are presented on open surfaces. A confined catalyst isolates these active species in a confined area. Molecules that will poison the catalyst cannot enter the isolated microenvironment, thus protecting the active substance from poisoning [22]. Transition metal oxide catalysts, such as MnO_x , FeO_x , and CoO_x , exhibited desirable activity in catalytic ozonation of VOCs [26,27]. The variable valence states and abundant oxygen vacancies contributed to their excellent performance in ozone decomposition, thus enhancing catalytic ozonation. This paper synthesized a popcorn-like zeolite-confined catalysts for catalytic ozonation of CH_3SH at room temperature. Mn, Fe, and Co were all investigated and Mn was selected as the optimal choice. The optimal catalyst attained complete conversion of CH_3SH at 15 °C with the $\text{O}_3/\text{CH}_3\text{SH}$ molar ratio of 1.33. Especially, it performed excellent stability at dry conditions and kept 70% of CH_3SH conversion with presence of 10 vol% H_2O at 15 °C. The confined structure was advantaged in sheet fusion morphology, micro-mesoporous channels with high surface area, strong metal-support interaction, abundant oxygen vacancies, superiority of adsorption capacity and surface acidity, thus contributing to excellent catalytic behaviors at low temperature. The oxidized products were also measured by an in-situ gas analyzer to reveal the conversion mechanism of CH_3SH with assistance of O_3 over this confined catalyst, hoping to provide new insights for the elimination of S-VOCs at room temperature.

2. Experimental methods

2.1. Synthesis of catalysts

2.1.1. Preparation of Mn-TEPA, Fe-TEPA and Co-EDA

The Mn-TEPA and Fe-TEPA solutions were prepared by dissolving 1.12 mL $\text{Mn}(\text{NO}_3)_2$ solution (50 wt%) and 1.92 g $\text{Fe}(\text{NO}_3)_2\cdot 9\text{H}_2\text{O}$ into 10 mL aqueous solution containing 0.96 mL tetraethylpentenamine (TEPA), respectively, and stirring to a transparent solution. The Mn-TEPA and Fe-TEPA solutions were used immediately after preparation, otherwise, it would settle down quickly. The Co-EDA solution was prepared by adding 1.31 g $\text{Co}(\text{NO}_3)_2\cdot 6\text{H}_2\text{O}$ into 10 mL water solution containing 0.3 mL ethylenediamine (EDA) and treating with ultrasonication for 30 min.

2.1.2. Synthesis of Mn@ZSM293, Fe@ZSM293 and Co@ZSM293

They were synthesized according to Yang et al. [16] with some modifications. 0.0544 g aluminum isopropyl alcohol and 8.13 mL tetrapropyl ammonium hydroxide solution (TPAOH, 2.0 M) were dissolved in 19 mL deionized water to attain ZSM293 with a $\text{SiO}_2/\text{Al}_2\text{O}_3$ ratio of 293. The optimal Mn proportion in Mn@ZSM293 comes from our previous paper [26]. The Mn-TEPA solution was then added to the mixture and stirred for 30 min. When the solution became clear, 8.32 mL tetraethyl orthosilicate (TEO) was added and stirred continuously for 12 h. The mixed solution was transferred to a 100 mL Teflon stainless steel autoclave and crystallized in a 170 °C oven for 72 h. After cooling to room temperature, the synthesized precipitates were centrifuged, washed three times, dried at 100 °C for 12 h, and finally calcined at 550 °C in air for 4 h with a heating rate of 1 °C/min. Fe@ZSM293 and Co@ZSM293 were synthesized similar to Mn@ZSM293, except that Mn-TEPA was replaced by Fe-TEPA and Co-EDA, respectively.

2.1.3. Synthesis of Mn/ZSM293, Fe/ZSM293 and Co/ZSM293

1.5 g prepared ZSM293 was added to Mn-TEPA and then transferred to a 100 mL beaker for water bath reaction, stirring at 70 °C until dry. After drying in oven at 100 °C, the solid product was calcined at 550 °C in the air for 4 h with a heating rate of 1 °C/min. Fe/ZSM293 and Co/ZSM293 were synthesized similar to those of Mn/ZSM293, except that Mn-TEPA was replaced by Fe-TEPA and Co-EDA, respectively.

In addition, the detailed synthesis of Mn@ZSM27, Mn@ZSM117 and Mn@ZSM400 was shown in the [Supplementary Information](#).

2.2. Catalyst characterization

The synthesized catalysts were characterized by high-resolution transmission electron microscope (HRTEM), scanning electron microscope (SEM), X-ray diffraction (XRD), Brunauer-Emmett-Teller (BET), X-ray photoelectron spectra (XPS), Raman spectra, pyrolysis-infrared spectroscopy (Py-IR), X-ray Fluorescence (XRF), H_2 temperature-programmed reduction ($\text{H}_2\text{-TPR}$), NH_3 temperature-programmed desorption ($\text{NH}_3\text{-TPD}$), Pyridine-IR spectra, O_2 temperature-programmed desorption ($\text{O}_2\text{-TPD}$), CH_3SH temperature-programmed desorption ($\text{CH}_3\text{SH-TPD}$) and Gasmet spectra, respectively. The detailed characterization procedures are same with our previous work [28]. Fourier transform infrared (FTIR) spectroscopy was carried out using VERTEX70 spectrometer (Bruker, GER) with 20 mg of fresh or spent catalyst. Pyrolysis gas chromatography-mass (Py-GCMS) spectra was pyrolyzed at 500 °C by Frontier 3030D pyrolysis analyzer, and then analyzed by QP2010ULTTA GC with 100 mg of spent catalyst.

The crystal sizes and crystallinity were calculated based on XRD results. The average crystal sizes were obtained using Scherrer equation $D = (K \times \lambda) / (\beta \times \cos \theta)$, where D is mean size of the ordered (crystalline) domains, K is Scherrer constant, λ is the X-ray wavelength, β is the line broadening at half the maximum intensity (FWHM), after correction, and θ is the Bragg angle (in radian). Generally, the area (A_s) obtained by the integration of the strongest diffraction peak is used A_s an

index to calculate the crystallinity, and the area (A_g) obtained by the integration of the standard material is compared, and the crystallinity = $A_s/A_g \times 100\%$.

2.3. Catalytic activity tests

Catalytic ozonation of CH_3SH was conducted in a self-designed platform that has described before [29]. The reactor is a continuous flow fixed bed quartz tube reactor (inner diameter of 8 mm and length of 500 mm), equipped with an electric heating furnace to control the reaction temperature. The reaction is carried out by filling the quartz tube with catalyst and quartz wool (thickness is 1 cm). CH_3SH was supplied by a cylinder gas (1000 ppm CH_3SH with N_2 balanced). Ozone was generated from a dielectric barrier discharger (HTU-500E) with O_2 input. The initial ozone concentration was measured by ozone concentration analyzer (BMT-964BT). The total gas flow rate was 100 mL/min and O_2 concentration was 5 vol%. Expect for specific investigation, the catalyst dosage was fixed at 25 mg, corresponding to a gas-time space velocity (GHSV) of 60000 h^{-1} ; the initial O_3 and CH_3SH input were 400 and 300 ppm, respectively, corresponding to a $\text{O}_3/\text{CH}_3\text{SH}$ of 1.33; the catalytic ozonation was conducted at 15 °C. Water vapor is produced by N_2 bubbling in a thermostatic bath. Water was injected into reaction system with N_2 bubbling at a certain temperature. The CH_3SH reaction products were monitored and analyzed online by gas chromatograph

(GC9790II). The CH_3SH reaction products were monitored and analyzed online by Fourier transform infrared spectroscopy gas analyzer (Gasmet, DX4000). The CH_3SH conversion was calculated by the following Eq. (1) to evaluate the catalytic activity. The turnover frequency (TOF) was calculated by the following Eq. (2) [30].

$$[\text{CH}_3\text{SH}]_{\text{conv.}} = (1 - [\text{CH}_3\text{SH}]_{\text{out}} / [\text{CH}_3\text{SH}]_{\text{in}}) \times 100\% \quad (1)$$

where the $[\text{CH}_3\text{SH}]_{\text{in}}$ and $[\text{CH}_3\text{SH}]_{\text{out}}$ are the CH_3SH inlet and outlet concentrations in ppm, respectively.

$$\text{TOF} = N / M (\text{h}^{-1}) \quad (2)$$

where N is the molar conversion of CH_3SH by per gram catalyst per second ($\text{mol} \cdot \text{g}^{-1} \cdot \text{h}^{-1}$), M is the catalyst active sites ($\text{mol} \cdot \text{g}^{-1}$).

3. Results and discussion

3.1. Morphologies of synthesized catalysts

As the morphologies depicted in Fig. 1, Mn@ZSM293 exhibits dramatically different structure compared with Mn/ZSM293. Generally, zeolite possesses much larger crystal size than MnO_x , ca. 90 ~ 300 and 20 ~ 60 nm, respectively. Therefore, the large massive particles in the HRTEM images are ZSM293 crystal, while the small dark particles are MnO_x nanoparticles. Clearly, MnO_x particles have blended into zeolite

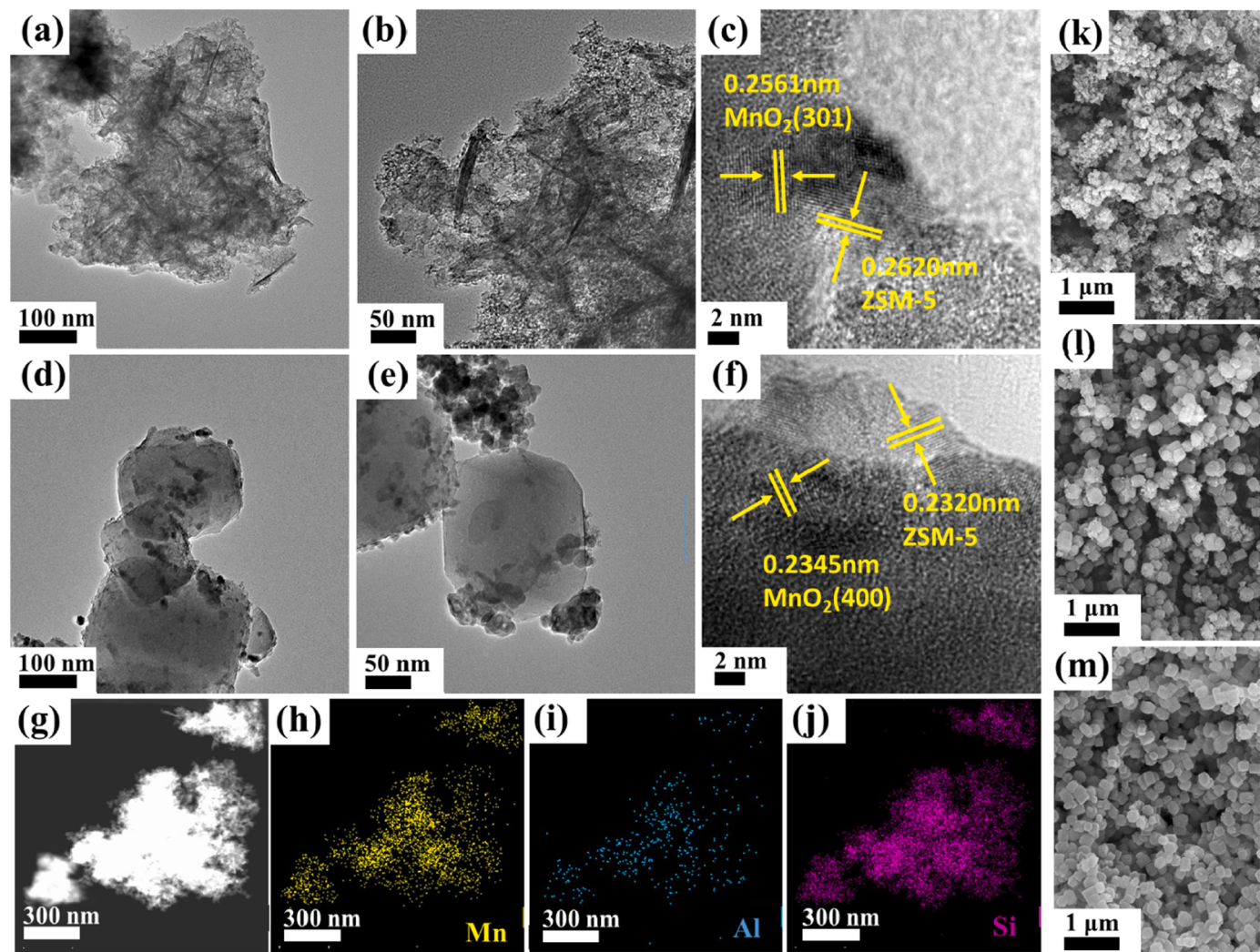


Fig. 1. HRTEM images of Mn@ZSM293 (a-c) and Mn/ZSM293 (d-f). EDS elemental maps of Mn@ZSM293 for Mn, Al and Si (g-j). SEM images of Mn@ZSM293 (k), Mn/ZSM293 (l) and ZSM293 (m).

crystals for Mn@ZSM293 with one-pot hydrothermal method, i.e., quite homogeneous dispersion of Mn and ZSM support (Fig. 1(a)~(b)), while the Mn particles are uniformly aggregated on the outer surface of the molecular sieve for Mn/ZSM293 with impregnation method (Fig. 1(d)~(e)). Compared with aggregation, homogeneous dispersion provides more exposed active sites of MnO_x for catalytic oxidation. Furthermore, the SEM images of Mn@ZSM293 display surface etching and collapse of the zeolite structure (Fig. 1(k)), which contributes to formation of oxygen vacancies. The collapse of zeolite structure can enhance the lattice distortion, which is more favorable for the formation of oxygen vacancy. Zhang et al. [31] prepared CeO_2 catalysts with different morphologies, and analyzed the correlation between the lattice distortion degree of CeO_2 and the concentration of oxygen vacancy, indicating that the lattice distortion degree of CeO_2 is linearly correlated with the concentration of oxygen vacancy. Besides, it has been reported that lattice distortion (such as interface dislocation and crystal deformation) is usually accompanied by oxygen vacancy [32,33]. Therefore, similar to popcorn, the collapsed structure is conducive to the dispersion and confinement of Mn species. By contrast, Mn/ZSM293 and ZSM293 consists of the prisms with a basic rule of shape (Fig. 1(l)~(m)). Therefore, Mn was successfully confined inside the molecular sieve crystals by one-pot hydrothermal method. The structures with well-defined large internal voids and surface etchings can capture

gaseous reactants and extend the retention time of the reactants, which are favorable for catalytic oxidation [34].

The lattice spacing can be measured from HRTEM images in Fig. 1(c) and Fig. 1(f). Mn@ZSM293 and Mn/ZSM293 exhibit 0.2561 and 0.2345 nm, corresponding to the typical (301) and (400) crystal plane of MnO_2 , respectively. Mn@ZSM293 and Mn/ZSM293 exhibit 0.2620 and 0.2320 nm corresponding to the ZSM-5, respectively. Precise elemental mappings of Mn@ZSM293 further demonstrate the uniform dispersion of Mn throughout zeolite structure in Fig. 1(g-j), indicating that Mn is confined to the molecular sieve structure. Meanwhile, HRTEM images of the other two confined catalysts Fe@ZSM293 and Co@ZSM293 shown in Fig. S1 also display no obvious observation of metal particle aggregation, validating confined effect.

3.2. Catalytic performance of CH_3SH ozonation

3.2.1. Catalytic behaviors over synthesized catalysts

Catalytic ozonation behaviors of CH_3SH are evaluated over these synthesized catalysts. Fig. 2(a) shows CH_3SH conversion over ZSM293 supported catalysts at 15 °C with $\text{O}_3/\text{CH}_3\text{SH}$ molar ratio of 1.33. As the benchmark, homogeneous ozonation of CH_3SH only exhibits less than 50% conversion but with good stability. The CH_3SH conversion rate of ZSM293 reaches 50% within 90 min, which is slightly higher than

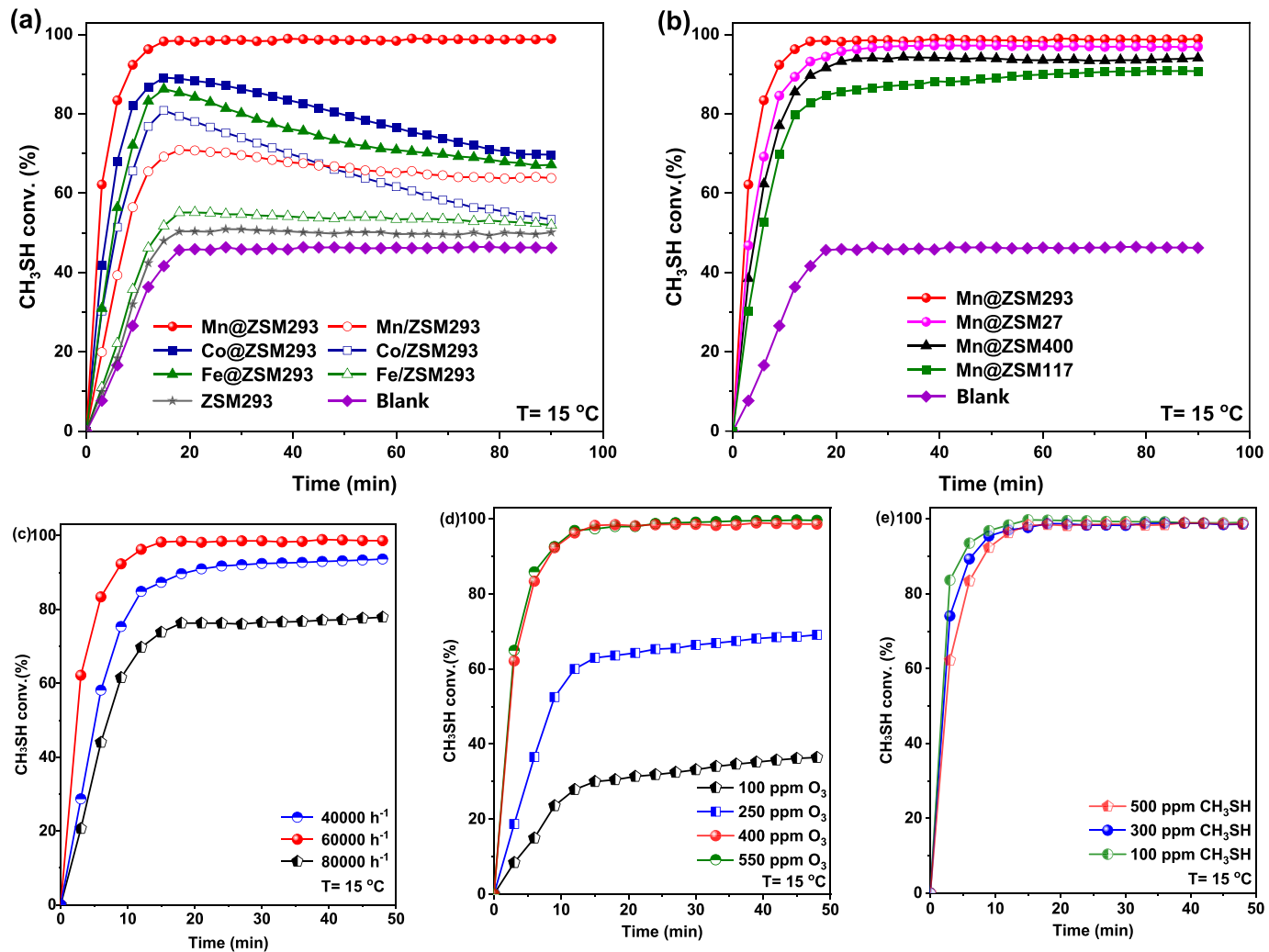


Fig. 2. Catalytic ozonation of CH_3SH at 15 °C over synthesized catalysts. Comparison between confined and impregnated catalysts for CH_3SH conversion (a); Effect of $\text{SiO}_2/\text{Al}_2\text{O}_3$ for CH_3SH conversion (b). (c) Effect of GHSV; (d) Effect of ozone inlet concentration (CH_3SH concentration: 300 ppm); (e) Effect of CH_3SH inlet concentration ($\text{O}_3/\text{CH}_3\text{SH}$: 1.33). Initial CH_3SH concentration: 300 ppm, $\text{O}_3/\text{CH}_3\text{SH}$: 1.33, 5 vol% O_2 , total gas flow rate: 100 mL/min, catalyst dosage: 0.025 g.

homogeneous ozonation. All these metal loading catalysts improve CH_3SH conversion and the catalysts with confined structure have dramatically higher CH_3SH conversion than the impregnated catalysts. CH_3SH conversion over Fe@ZSM293 increases 30% compared with that over Fe/ZSM293 and maximizes at 88%, but it deactivates quickly to 70% after 90 min. Co loading catalysts display same deactivation for both Co@ZSM293 and Co/ZSM293 , while they also slightly surpass the corresponding Fe loading catalysts. Fortunately, Mn/ZSM293 displays not so high CH_3SH conversion but possesses good stability with a function of time and Mn@ZSM293 attains 100% CH_3SH conversion with no deactivation. The ozone residue for catalytic ozonation over Mn@ZSM293 at 1.33 is 38 ppm, which is less than homogeneous ozonation, ca. 103 ppm. Therefore, catalysts can improve the utilization rate of ozone and reduce the ozone residue. Overall, confined structure indeed improves catalytic ozonation of CH_3SH for Mn, Co and Fe loading catalysts. Mn@ZSM293 finally reaches complete conversion of CH_3SH and can be selected as the optimal catalyst for further investigation. Considering that the $\text{SiO}_2/\text{Al}_2\text{O}_3$ ratio of zeolite is also one of the factors affecting the reactivity [26], Mn@ZSM catalysts with varied $\text{SiO}_2/\text{Al}_2\text{O}_3$ ratios, ca. 27, 117, 293 and 400, are evaluated for catalytic ozonation of CH_3SH , as shown in Fig. 2(b). Clearly, all these catalysts are good candidates for CH_3SH ozonation with high conversion and stability. In comparison, CH_3SH conversion declines as the order: $\text{Mn@ZSM293} > \text{Mn@ZSM27} > \text{Mn@ZSM400} > \text{Mn@ZSM117}$. Generally, lower $\text{SiO}_2/\text{Al}_2\text{O}_3$ ratio implies higher acidity. The uncertain variation demonstrate suitable acidity is favorable for catalytic ozonation of CH_3SH despite weak effect from $\text{SiO}_2/\text{Al}_2\text{O}_3$ ratio of zeolite.

3.2.2. Effect of catalytic parameters

Next, the effect of gas hour space velocity (GHSV), O_3 input and CH_3SH concentration on catalytic behaviors are investigated over Mn@ZSM293 . As shown in Fig. 2(c), CH_3SH conversion first increases from 94% to 99% with elevation of GHSV from 40,000 to 60,000 h^{-1} , while it further declines to 79% when the GHSV reaches 80,000 h^{-1} . Catalytic ozonation involves ozone decomposition and CH_3SH oxidation, therefore the balance between these two steps determines CH_3SH conversion. Low GHSV with more catalyst dosage promotes CH_3SH adsorption and oxidation, but it also causes too rapid ozone decomposition that will provide insufficient oxidizing radicals for CH_3SH oxidation. Hereafter, 60,000 h^{-1} is selected as the optimal GHSV for further investigation. Fig. 2(d) reflects CH_3SH conversion with function of O_3 input at same initial CH_3SH concentration of 300 ppm. CH_3SH conversion elevates significantly from 38% to 99% when ozone inlet concentration increases from 100 to 400 ppm, corresponding to the $\text{O}_3/\text{CH}_3\text{SH}$ molar ratio of 0.33–1.33. However, further increase in ozone concentration from 400 to 550 ppm exhibits excessive input that has negligible effect on CH_3SH conversion. Therefore, the optimal $\text{O}_3/\text{CH}_3\text{SH}$ molar ratio for Mn@ZSM293 catalytic ozonation of CH_3SH is selected as 1.33, which is the lowest value compared with previous reports. Previous literature reported a higher $\text{O}_3/\text{CH}_3\text{SH}$ molar ratio for such high removal efficiency, ca. 2.5 [5]. The confined structure of Mn@ZSM293 should contribute to this desirable catalytic ozonation activity. However, CO selectivity gradually increases with elevation of $\text{O}_3/\text{CH}_3\text{SH}$, while CO_2 selectivity exhibits decreasing tendency. Catalytic ozonation of CH_3SH still faces with the problem of CO production and undesirable mineralization rate. In terms of the initial concentration of CH_3SH , lower value displays faster elevation of conversion as a function of time with same $\text{O}_3/\text{CH}_3\text{SH}$ of 1.33 at 15 °C, as shown in Fig. 2(e). Nevertheless, when the initial CH_3SH concentration increases from 100 to 500 ppm, the final stable CH_3SH conversion all reached 99%. To evaluate the activation energy of CH_3SH oxidation over these catalysts, Arrhenius plots obtained from experiments under low CH_3SH conversion are presented in Fig. S4. Activation energy E_a is calculated to be ZSM293 (36.44 $\text{kJ}\cdot\text{mol}^{-1}$) > Mn/ZSM293 (33.91 $\text{kJ}\cdot\text{mol}^{-1}$) > Mn@ZSM293 (20.86 $\text{kJ}\cdot\text{mol}^{-1}$). Clearly, Mn@ZSM293 has the lowest E_a value, which confirms its superior activation performance in CH_3SH

oxidation. $\text{TOF}_{\text{Mn@ZSM293}}$ is 1764 h^{-1} , much higher than $\text{TOF}_{\text{Mn/ZSM293}}$, which is 1116 h^{-1} in Fig. S10. Mn@ZSM293 has stronger catalytic activity for the ozonation of CH_3SH , and the TOF is about 1.6 times that of Mn/ZSM293 , indicating that confined catalyst has strong catalytic activity. Fig. S5 reflects that CO occupies more proportion than CO_2 with the elevation of CH_3SH conversion rate by increasing O_3 input. How to control the products is still a big challenge.

3.2.3. Catalyst stability

CH_3SH contains sulfur that usually causes poisoning effect on catalyst, which has been reported previously for catalytic oxidation of sulfur-containing VOCs [13]. Fortunately, Mn@ZSM293 exhibits excellent stability for almost complete CH_3SH ozonation within 24 h at 15 °C (Fig. 3(a)). This is quite good performance compared with Mn/ZSM293 , which has an initial CH_3SH conversion of 70% and then gradually declines to 52%. Next, the water resistance of Mn@ZSM293 for CH_3SH catalytic ozonation was investigated with the O_3/DCM of 1.33. Fig. 3(b) demonstrates CH_3SH conversion with switching different water content at 15 °C. CH_3SH conversion decreases quickly from 99% to approximately 70% with introduction of 1 vol% H_2O for 90 min. Water removal indeed recovers CH_3SH conversion a lot, but it only reaches 80%. Next, CH_3SH conversion declines to approximately 70% again after adding 5 vol% H_2O for 90 min. Clearly, this deactivation is very weak compared with the previous stage of 1 vol% H_2O . After the water is stopped, the activity increases slightly but still cannot return back to 70%. Interestingly, introduction of 10 vol% H_2O causes negligible decrease and even slight increase of CH_3SH conversion, which finally stabilizes at ~73% after 90 min. Generally, presence of water with stronger adsorption energy occupies oxygen vacancies and prevents electron transfer, which should be the dominant reason for deactivation [35]. Besides, water presence also promotes sulfates deposition with higher stability on catalyst surface, which should be the second reason for deactivation. Nevertheless, the portion of H_2O can decompose into hydroxyl radicals at active sites, which promotes catalytic ozonation [36]. After water removal and regeneration through 5 h purging with dry N_2 , the activity of Mn@ZSM293 catalyst for ozonation of CH_3SH is shown in Fig. S8, and the catalytic conversion rate can be restored to 98%. Overall, Mn@ZSM293 exhibits good water resistance that can stabilize at ~70% with presence of high concentration of water vapor for a long time and the catalyst activity can be restored after the removal of water.

3.2.4. Effect of temperature and water vapor

To systematically investigate the effect of temperature and water vapor on catalytic ozonation of CH_3SH , stage temperature programmed experiments are conducted with varied $\text{O}_3/\text{CH}_3\text{SH}$ and water content, as depicted in Fig. 3(c). Expect for catalyst, temperature is the most critical factor affecting CH_3SH conversion. Clearly, CH_3SH conversion with homogeneous ozonation elevates step by step from 15 to 150 °C. Initially, blank condition with $\text{O}_3/\text{CH}_3\text{SH}$ of 0.67 only attains ~30% CH_3SH conversion at 15 °C, but it finally reaches ~90% at 150 °C. Temperature rising becomes the dominant power promoting CH_3SH ozonation. In comparison, catalytic ozonation over Mn@ZSM293 attains 60–70% CH_3SH conversion at 15 °C with same O_3 input and reaches 95% at 100 °C. When the $\text{O}_3/\text{CH}_3\text{SH}$ increases to 1.33, higher CH_3SH is observed for blank condition but it still cannot surpass catalytic ozonation with $\text{O}_3/\text{CH}_3\text{SH}$ of 0.67. Because catalytic ozonation with $\text{O}_3/\text{CH}_3\text{SH}$ of 1.33 has attained 100% CH_3SH conversion, it is not shown here for varied temperature. Therefore, the promotion effect from Mn@ZSM293 is mainly reflected at lower temperature, i.e., 100% CH_3SH conversion at 15 °C with Mn@ZSM293 , while only 45% CH_3SH conversion without catalyst at same $\text{O}_3/\text{CH}_3\text{SH}$ of 1.33. When water is introduced, the superiority of Mn@ZSM293 can be further strengthened. Firstly, CH_3SH conversion is no longer rising when temperature increases from 75 to 100 °C for blank condition with 10 vol% H_2O . It finally stabilizes at 40% for the rest of temperature ranges. Secondly, although Mn@ZSM293 also exhibits deactivation at high temperature

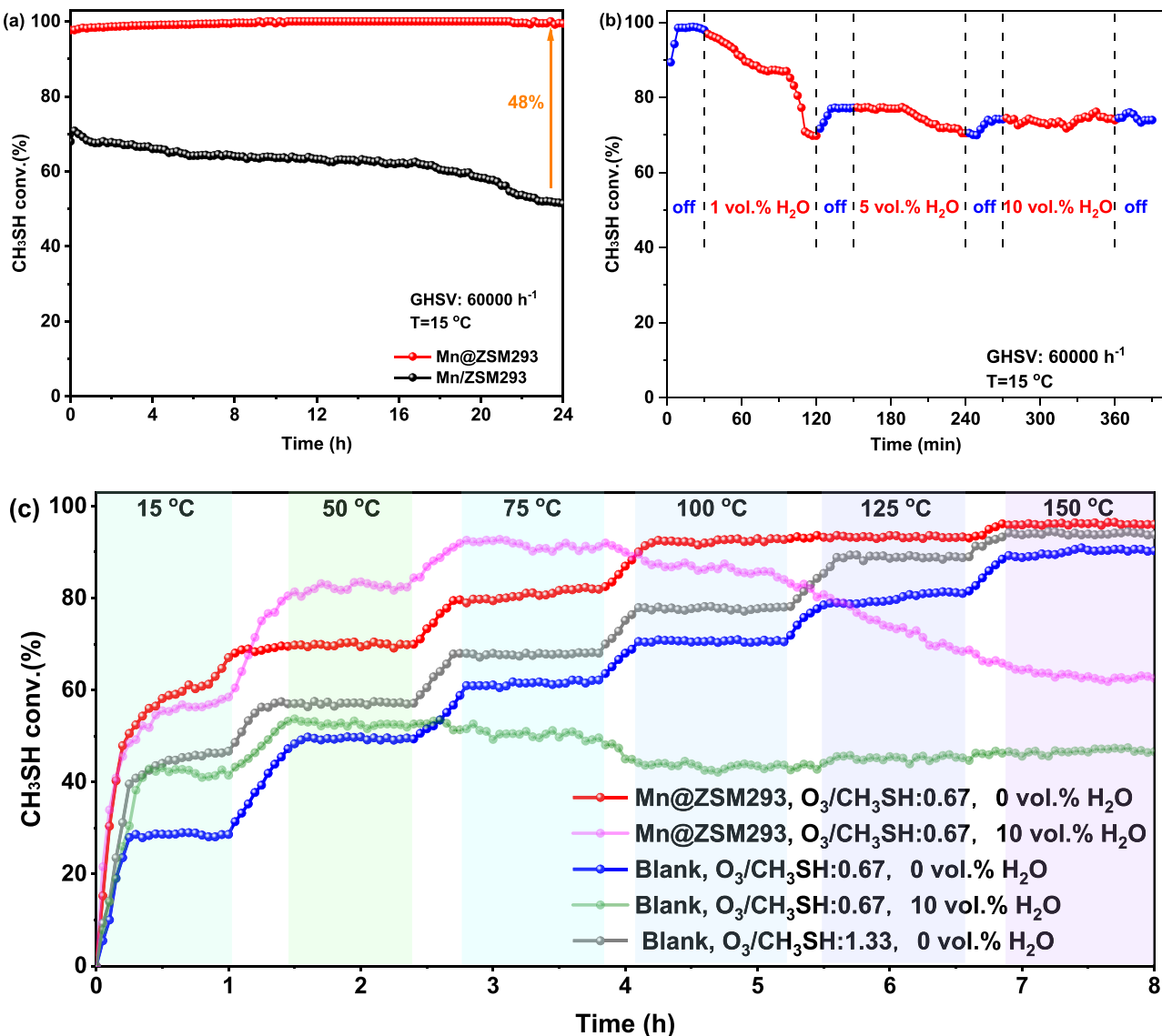


Fig. 3. (a) Long-term stability of CH₃SH ozonation at 15 °C; (b) Water durability tests; (c) Temperature programming conversion of CH₃SH in different system. Initial CH₃SH concentration: 300 ppm, O₃/CH₃SH:1.33, 5 vol% O₂, total gas flow rate: 100 mL/min, catalyst dosage: 0.025 g.

with presence of water, CH₃SH conversion is much higher compared with blank condition. Interestingly, for both blank condition and catalytic ozonation, water presence promotes CH₃SH conversion firstly at low temperature ranges. To some extent, initial water addition may have a low content in the reaction system that the positive effect surpasses the negative effect. H₂O dissociation with assistance of O₃ generating abundant hydroxyl radicals contributes to this promotion effect. At the same time, a small amount of H₂O helps to migrate the reaction intermediates and products from the catalyst, avoiding their accumulation on the surface. However, whether blank conditions or catalytic ozonation, the presence of water inhibits the conversion of CH₃SH in the high temperature range. Therefore, it cannot be attributed to the competitive effect from H₂O adsorption over catalyst. To some extent, higher temperature might promote ozone decomposition with presence of H₂O without participating into catalytic ozonation of CH₃SH. The formation of hydroxyl radicals cannot offset the promotion on ozone decomposition.

3.3. Crystalline, textural, and surface properties

3.3.1. XRD patterns and Raman spectra

Both Mn/ZSM293 and Mn@ZSM293 have clear diffraction peaks belonging to the crystal structure of ZSM293, as shown in Fig. 4(a). The results indicate that the zeolite crystal structure cannot be changed by either the metal confinement or impregnation [27]. Crystallite dimension and crystallinity of ZSM293 calculated by XRD patterns are supplemented in Table S2. Mn@ZSM293 possesses the lowest crystallinity and crystal diameter, indicating more disordered crystals and defects, which is also consistent with the results of popcorn-like morphology in the SEM images (Fig. 1(k)). Other metal loading also presents same diffraction peaks in Fig. S2. Interestingly, Fe loading causes dramatic decrease in the intensity of diffraction peaks, especially for Fe@ZSM293, suggesting severe interaction [37]. Because of low metal loading and high dispersion, no obvious characteristic peaks with Mn, Fe, and Co can be detected. Fig. 4(b) shows the Raman spectra of Mn@ZSM293 and Mn/ZSM293. The single prominent peak at 634 and 614 cm⁻¹ can be identified as the vibration of ZSM293 crystal. The peak of Mn@ZSM293 shifts towards lower wavenumber and exhibits weaker intensity but wider range. It shows that Mn confined in ZSM293, there is strong

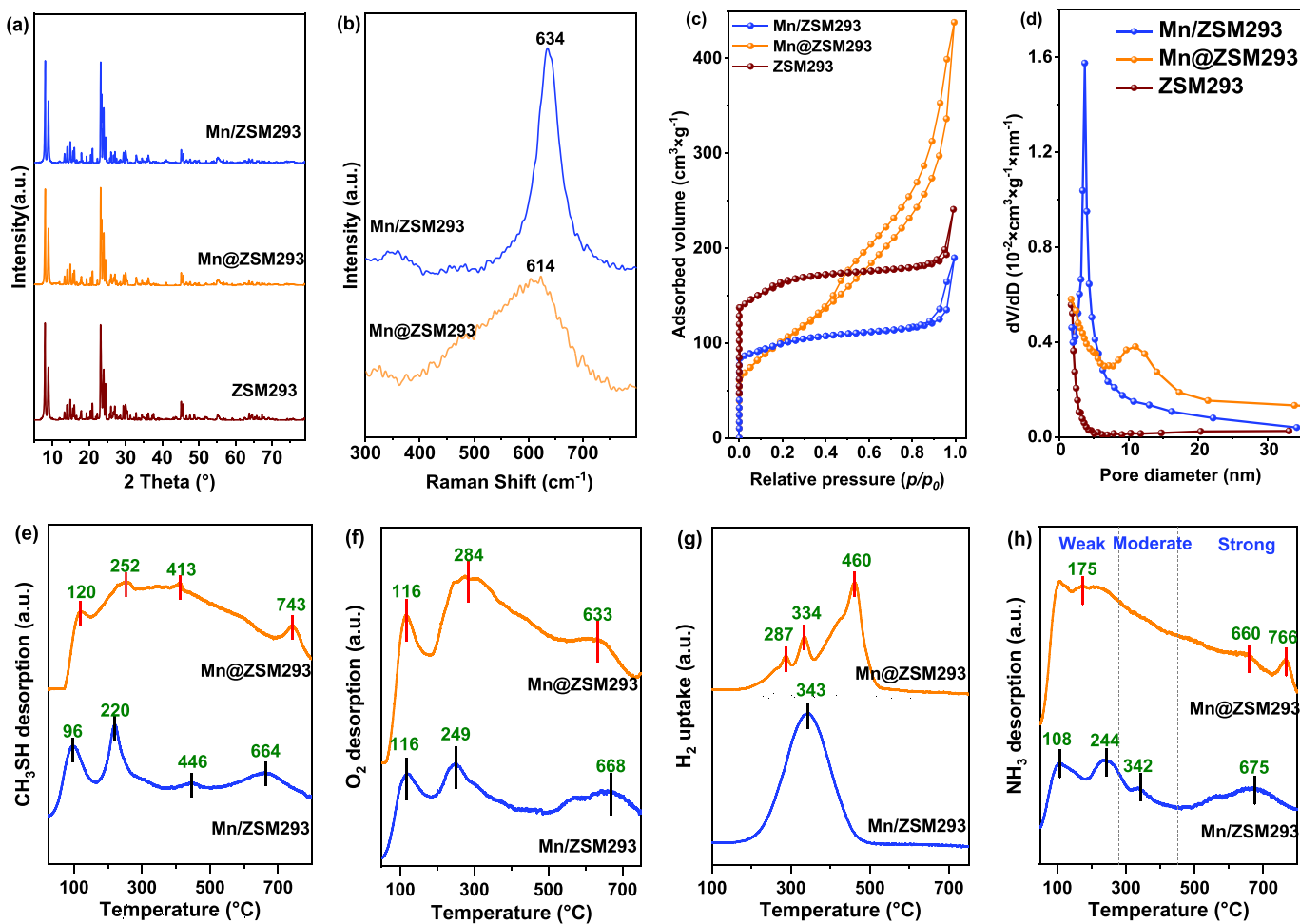


Fig. 4. (a) XRD patterns; (b) Raman spectra; (c) N_2 adsorption-desorption isotherms; (d) Pore size distribution; (e) CH_3SH -TPD profiles; (f) O_2 -TPD profiles; (g) H_2 -TPR profiles.

interaction between Mn and ZSM293 [13]. The strong metal-support interaction (SMSI) optimizes the surface oxygen species and oxygen mobility of the catalyst, promotes electron transfer, and thus obtains higher apparent activity [38].

3.3.2. Textural properties

Zeolite based catalysts are rich in microporous structure, which is beneficial to adsorb gas molecules during catalytic ozonation. Besides, metal loading further introduced mesoporous structure that can promote diffusion of reactants and products, thus enhancing transformation and desorption of intermediates and final products. The nitrogen adsorption-desorption isotherms and BJH pore size distribution curves (PSD) of Mn/ZSM293, Mn@ZSM293 and ZSM293 are shown in Fig. 4(c) ~ (d). Other catalysts are presented in Fig. S3. The pore structure parameters of these five catalysts are tabulated in Table 1. Clearly, ZSM293 exhibits a rapid increase in adsorbed volume at $p/p_0 = 0.0$, and shows a relatively stable trend at $p/p_0 < 0.8$, and finally elevates a lot at high relative pressure. This corresponds to type I isotherms and H4 hysteresis loop, indicating microporous structure [39]. Mn loading by impregnated method on ZSM293 presents lower increase in the first and second stage, but has a bigger H4 hysteresis loop than pure ZSM293, implying larger pore size. Fig. 4(d) also confirms this variation that a peak intensity is observed at ~ 5 nm for Mn/ZSM293. The average pore diameter is calculated to be 5.5 nm, which is slightly larger than ZSM293, ca. 5.0 nm. Mn@ZSM293 displays a significantly different shapes that the hysteresis loop should ascribe to H3 type, corresponding to the sheet

Table 1
Textural properties and chemical composition of the catalysts.

Catalyst	BET surface area (m ² /g)	Total pore volume ^a (cm ³ /g)	Average pore diameter ^b (nm)	Metal loading ^c (wt %)
ZSM293	514.0	0.24	5.0	0
Mn@ZSM293	601.5	0.59	7.2	10.0
Mn/ZSM293	310.6	0.31	5.5	9.6
Fe@ZSM293	494.0	0.50	7.6	9.5
Fe/ZSM293	435.6	0.35	5.9	10.3
Co@ZSM293	456.9	0.56	7.2	10.0
Co/ZSM293	369.0	0.32	6.7	10.2

^a Total pore volume of $P/P_0 = 0.95$.

^b BJH desorption average pore diameter.

^c Determined by ICP-AES analysis.

structure which has been verified in TEM images (Fig. 1(a)). The larger hysteresis loop of Mn@ZSM293 also contributes to its high surface area, ca. 601.5 m²/g. Besides, Mn@ZSM293 also possesses wider pore size distribution from 0 to 20 nm, and the average pore diameter is much higher than ZSM293, ca. 7.5 > 5.0 nm. Interestingly, Fe and Co confined catalysts also present similar tendency. The pore structure parameters of these five catalysts are tabulated in Table 1. The specific surface area of Mn@ZSM293 catalyst is higher than that of Co@ZSM293 and Fe@ZSM293. The larger specific surface area is conducive to the contact reaction between the active site on the catalyst surface and CH_3SH . At

the same time, the HRTEM of Fe@ZSM293 and Co@ZSM293 are shown in Fig. S1. The metal dispersion of Co and Fe is general, and there are more agglomerated nanoparticles, while Mn is well dispersed in the popcorn-like structure and pores. These phenomena demonstrate that this confined structure obviously widens the pore channels of zeolite and creates more mesoporous channels, which contributes to their better CH₃SH catalytic ozonation performance.

3.3.3. Surface properties

Fig. 4(e)~(h) exhibit the adsorption, reducibility and acidity of Mn@ZSM293 and Mn/ZSM293. CH₃SH desorption profiles shown in Fig. 4(e) clearly present that Mn@ZSM293 possesses much higher adsorption capacity of CH₃SH than Mn/ZSM293. A wide desorption is occurred from 80 to 800 °C without any interval for Mn@ZSM293, while Mn/ZSM293 mainly has two desorption peaks at 96 and 220 °C. The desorption amount can be semiquantitatively calculated by integrated area of desorption profiles. Mn@ZSM293 possesses 2.13 times higher than Mn/ZSM293. Besides, Mn@ZSM293 exhibits stronger CH₃SH desorption due to the stronger peak at higher temperature range, ca. 300–500 °C, contributing to higher conversion with low O₃ input, i.e., higher O₃ utilization rate. In general, the decomposition of O₃ follows the order of adsorption and activation on oxygen vacancies [40]. Intermediates of CH₃SH may be deposited at the active site, which is not conducive to oxygen vacancy formation and oxygen migration [41]. The O₂-TPD curves shown in Fig. 4(f) also exhibit similar tendency that Mn@ZSM293 has much higher desorption amount than Mn/ZSM293, ca. 2.29 times. O₂-TPD can be used to evaluate oxygen adsorption capacity and oxygen mobility. Generally, O₂ desorption profiles can be roughly divided into three types, namely surface adsorbed oxygen (O_{ads}, < 200 °C), surface lattice oxygen (O_{s-latt}, 200 ~ 600 °C) and bulk lattice oxygen (O_{b-latt}, > 600 °C) [42]. Clearly, the contents of O_{ads} and O_{s-latt} of Mn@ZSM293 are both higher than that of Mn/ZSM293, indicating more abundant surface oxygen species with higher mobility. High dispersion of Mn oxides in this confined structure should correlate to this phenomenon. Therefore, Mn@ZSM293 possesses more active sites for catalytic ozonation of CH₃SH. The reducibility of the catalyst can be reflected by H₂-TPR profiles shown in Fig. 4(g). Definitely, the H₂ uptake mainly originates from step reduction of MnO_x, i.e., MnO₂ to Mn₂O₃, Mn₃O₄ and MnO in sequence [43]. Clearly, Mn/ZSM293 possesses one single reduction peak centralized at 343 °C, while Mn@ZSM293 has three reduction peaks at 287, 334 and 460 °C. Especially, the total H₂ uptake of Mn@ZSM293 is lower than that of Mn/ZSM293, ca. 0.77 times. On one hand, Mn@ZSM293 with confined structure implies deep fusion of MnO_x into zeolites, contributing to strong metal support interaction (SMSI) and thus generating multiple reduction peaks. Besides, the temperatures of the first two reduction peaks for Mn@ZSM293 are lower than that for Mn/ZSM293, implying better reducibility at lower temperature. On the other hand, because the practical Mn loading on these two catalysts are similar as tabulated in Table 1, the low H₂ uptake should correlate to the lower valance state of MnO_x in Mn@ZSM293 than that in Mn/ZSM293, which can be reflected in Table 2. NH₃-TPD profiles shown in Fig. 4(h) clearly present surface acidity of catalysts. Generally, the NH₃-TPD distribution can be divided into weak (< 280 °C), moderate (280–450 °C) and strong acidity (> 450

°C) [44]. Both Mn@ZSM293 and Mn/ZSM293 have obvious desorption peaks at low temperature, corresponding to weak acidity. Dramatically, Mn@ZSM293 has much wider desorption peak in the whole temperature range, while Mn/ZSM293 possesses three obvious peaks in the temperature range of weak and moderate acidity. However, the strong acidity of Mn@ZSM293 at 660 and 766 °C is weaker than that of Mn/ZSM293 at 675 °C. Too strong acidity usually has a negative impact on catalytic ozonation [45]. It was reported that strong acid sites cause excessive breakage of C–S bonds, thus promoting accumulation of sulfur/coke deposits and leading to deactivation [8]. Table S1 and Fig. S7, specifically describes the types and quantities of acidic sites through Py-IR measurement results. Mn@ZSM293 has the highest Bronsted acidic sites and Lewis acidic sites, 5.18 and 68.6 $\mu\text{mol}\cdot\text{g}^{-1}$, respectively, while the Bronsted acidic sites of Mn/ZSM293 almost disappear. The ratio of Bronsted acid sites to Lewis acid sites (B/L) is also much higher than that of Mn/ZSM293. Ozone is generally adsorbed on the Lewis acid sites and decomposed into surface atomic oxygen species and active oxygen radicals, but ozone is electrostatically adsorbed on the Brønsted acid sites without effective decomposition and just directly participate into catalytic reactions with original ozone molecules [46]. However, more Brønsted acid sites imply strong proton supply capacity [47], which is conducive to the adsorption of CH₃SH, activation and breakage C–C and C–S bonds. Extremely strong acidity (Brønsted acidity) will cause excessive decomposition of C–S bonds and therefore leads to sulfur/coke deposition [8]. Therefore, the distinct superiority in weak and moderate acidity of Mn@ZSM293, as well as abundant Bronsted acidic sites should be the crucial contributions for catalytic ozonation [48]. Therefore, the distinct superiority in weak and moderate acidity of Mn@ZSM293, as well as abundant Brønsted acidic sites should be the crucial contributions for catalytic ozonation.

3.3.4. Elemental distribution

The elemental states of Mn, O and S are determined by XPS. Expect for Mn@ZSM293 and Mn/ZSM293, the spent Mn/ZSM293 after catalytic ozonation of CH₃SH for 90 min at 15 °C with O₃/CH₃SH of 1.33 are also investigated for comparison. The XPS spectra of Mn 2p, Mn 3 s, O 1 s and S 2 s are deconvoluted by Gaussian functions as shown in Fig. 5 (a)~(d), and the ratios calculated by integrated area are tabulated in Table 2. Mn 2p_{3/2} spectra are deconvoluted into three peaks, corresponding to Mn(IV), Mn(III) and MnO satellite from low to high binding energies, respectively. The MnO satellite peak is only observed for Mn@ZSM293, which should originate from low oxidation degree of MnO_x due to encapsulation into ZSM structure without contact with O₂. This phenomenon also demonstrates that presence of SMSI between MnO_x and ZSM293 for this confined catalyst. In comparison, Mn@ZSM293 present lower Mn⁴⁺ proportion than Mn/ZSM293 (Table 2). In addition, the average oxidation state (AOS) of Mn 3 s is calculated according to Mn 3 s spectra (Fig. 5(b)) with the formula AOS = 8.956 – 1.126ΔEs, where ΔEs represents the difference in binding energy between the two Mn 3 s peaks [49]. Clearly, the AOS of fresh Mn@ZSM293 is significantly lower than that of fresh Mn/ZSM293, ca. 2.2 < 2.6 (Table 2). This result is consistent with the presence of MnO and lower proportion of Mn⁴⁺ from Mn 2p spectra. The Jahn-Teller distortion occurs with more low-priced Mn species presented in MnO₂, creating oxygen vacancies to maintain charge conservation [50]. This contributes to better catalytic ozonation of CH₃SH over Mn@ZSM293. The spent Mn@ZSM293 displays slightly higher AOS than the fresh one due to ozone oxidation. This might imply that catalytic ozonation involves MvK mechanism. O 1 s XPS spectra in Fig. 5(c) are assigned into two components with binding energies of 530.39 and 528.45 eV of Mn@ZSM293, respectively, corresponding to adsorbed oxygen (O_{ads}) and lattice oxygen (O_{lat}) [51]. Interestingly, Mn@ZSM293 displays a certain variation compared with Mn/ZSM293 in terms of the binding energies. That is, O 1 s spectra shifts towards higher binding energy, while Mn 2p spectra moves to lower value, indicating strong interaction between Mn and O atom in Mn@ZSM293 [52], which is consistent with

Table 2

Surface compositions of Mn and O for fresh Mn/ZSM293, fresh and spent Mn@ZSM293 based on XPS results.

Catalyst	Mn ⁴⁺ (%)	Mn ³⁺ (%)	MnO (%)	AOS	O _{ads} (%)	O _{lat} (%)
Fresh Mn@ZSM293	52.7	36.6	10.7	2.2	89.5	10.5
Fresh Mn/ZSM293	55.2	44.8	/	2.6	79.4	20.6
Spent Mn@ZSM293	51.2	36.2	12.6	2.3	84.0	16

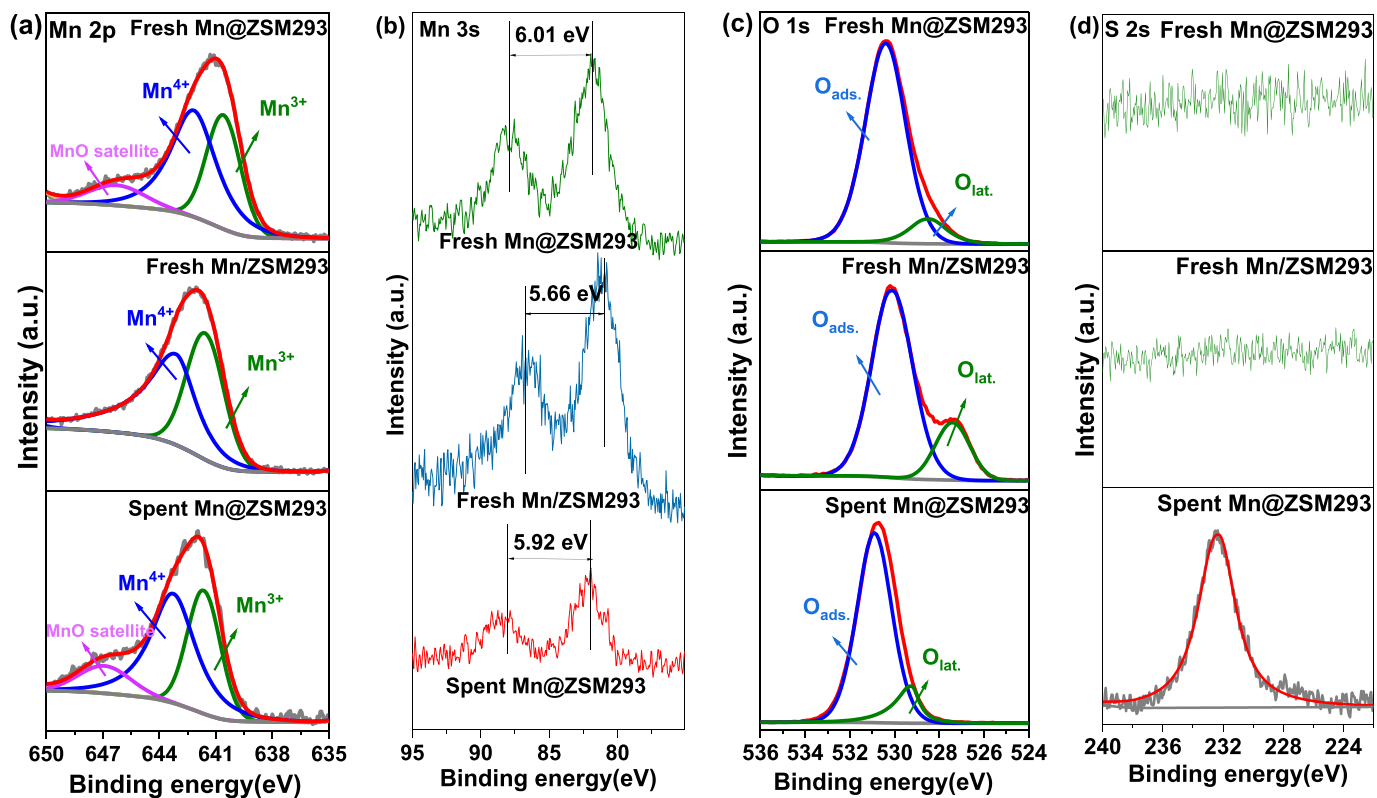


Fig. 5. (a) XPS spectra of Mn 2p_{3/2}; (b) XPS spectra of Mn 3 s; (c) XPS spectra of O 1 s; (d) XPS spectra of Mn 2p.

the results of TEM in Fig. 1, Mn exists in the form of manganese oxide. Clearly, Mn@ZSM293 has a higher proportion of O_{ads.} than Mn/ZSM293, ca. 89.5% > 79.4% (Table 2), which includes OH⁻, O⁻ and O²⁻, thus enhancing catalytic ozonation of CH₃SH [53]. Interestingly, O_{ads.} were reduced after catalytic ozonation, indicating that the catalytic ozonation of CH₃SH would consume O_{ads.} As expected, sulfate species are detected on the surface of spent Mn@ZSM293. However, sulfate deposition causes no deactivation as presented in Fig. 3(a). Our previous research also found that catalytic ozonation exhibited excellent activity even with sulfur deposition [54].

3.4. Mechanism for the oxidation of CH₃SH over Mn@ZSM293

The tail gas is detected using Gasmet to identify varied products from catalytic ozonation of CH₃SH over Mn@ZSM293. Fig. 6(a) presents the outlet gas from homogenous ozonation of CH₃SH without catalyst with total gas flow rate of 500 mL/min. Clearly, ozone injection causes some bands appear near 2663–3111 cm⁻¹, which were all generated by the transformation of CH₃SH to CH₃S⁻. Besides, a new peak formed at 1204 cm⁻¹ is methyl sulfonic acid (CH₃SO₃H). These two species gradually decrease with the elevation of temperature, indicating that CH₃SH is converted to CH₃S⁻ and CH₃SO₃⁻ by partial S–H bond rupture with ozone at low temperature and further transformed to other compounds at high temperature [12]. With the increase of temperature, SO₂ bands (1376 and 1343 cm⁻¹), HCOO⁻ bands (1598 cm⁻¹), and sulfate bands (SO₄²⁻, 1065 cm⁻¹) appear and continuously increase, indicating that C–S and S–S bonds in CH₃SO₃⁻ were broken and converted to SO₂, SO₄²⁻, and HCOO⁻ [5]. Fig. 6(b) presents similar experiment results with variation of total gas rate to 200 mL/min. Obviously, HCOO⁻ groups are observed at 1698 and 1544 cm⁻¹ with stronger peak intensities. SO₂ also displays similar tendency, which reflects the increased conversion rate of CH₃SH and the more thorough oxidation. This indicates that longer retention time promotes CH₃SH ozonation.

Fig. 6(c)~(d) display the infrared spectra of outlet gas from CH₃SH catalytic ozonation over Mn@ZSM293 and Mn/ZSM293, respectively. Before ozone injection, the peak intensity at 1698, 1544, and 1088 cm⁻¹ is higher than that without catalyst, indicating that CH₃SH also partially reacts with the surface of the catalyst to generate HCOO⁻ and SO₄²⁻ without ozone. The peak intensities of deprotonated and protonated sulfonic acid (CH₃SO₃H and CH₃SO₃⁻) located at 1165 and 1189 cm⁻¹ increase significantly for Mn@ZSM293, indicating that CH₃S⁻ is effectively oxidized to CH₃SO₃⁻. At the same time, gas bands assigned to HCOO⁻ at 1698 and 1544 cm⁻¹, SO₂ at 1376 and 1343 cm⁻¹, and SO₄²⁻ at 1088 cm⁻¹ show significant elevation in band strength, indicating that CH₃SO₃⁻ is further oxidized to carboxylic acid (HCOO⁻), SO₂, and SO₄²⁻. The conversion rate was significantly improved by the addition of catalysts. In comparison, the signal strength of the oxidation products over the confined catalyst increases faster and stronger than that over the impregnated catalyst. The results show that the reaction path of confined and impregnated catalysts was similar, and different catalysts mainly affected the activity. Catalytic ozonation of CH₃SH with presence of 1 vol% H₂O over Mn@ZSM293 is shown in Fig. S6. The signals at 2123–1165 cm⁻¹ originating from H₂O adsorption are too obvious and cover up other signals. Py-GC/MS spectra of the Mn@ZSM293 for byproducts distribution analysis after catalytic ozonation of CH₃SH is shown in Fig. S11, and Table S4. Three by-products are remained on the catalyst surface, including methanesulfonic acid, dimethyl sulfone and methane. Methanesulfonic acid is CH₃SO₃⁻, intermediate product of ozonation of CH₃SH, which is also consistent with the results of Gasmet. CH₄ and C₂H₆O₂S are byproducts of incomplete ozonation deposited on the catalyst surface. The accumulation of products and intermediates on the surface of Mn@ZSM293 after reaction for 12 h was further investigated by FTIR (Fig. S9). Only a small amount of carbon and sulfur groups are observed compared with the fresh catalyst, indicating that the number of residual products and intermediates on the catalyst surface was small. This is also consistent with the few intermediate results in Py-

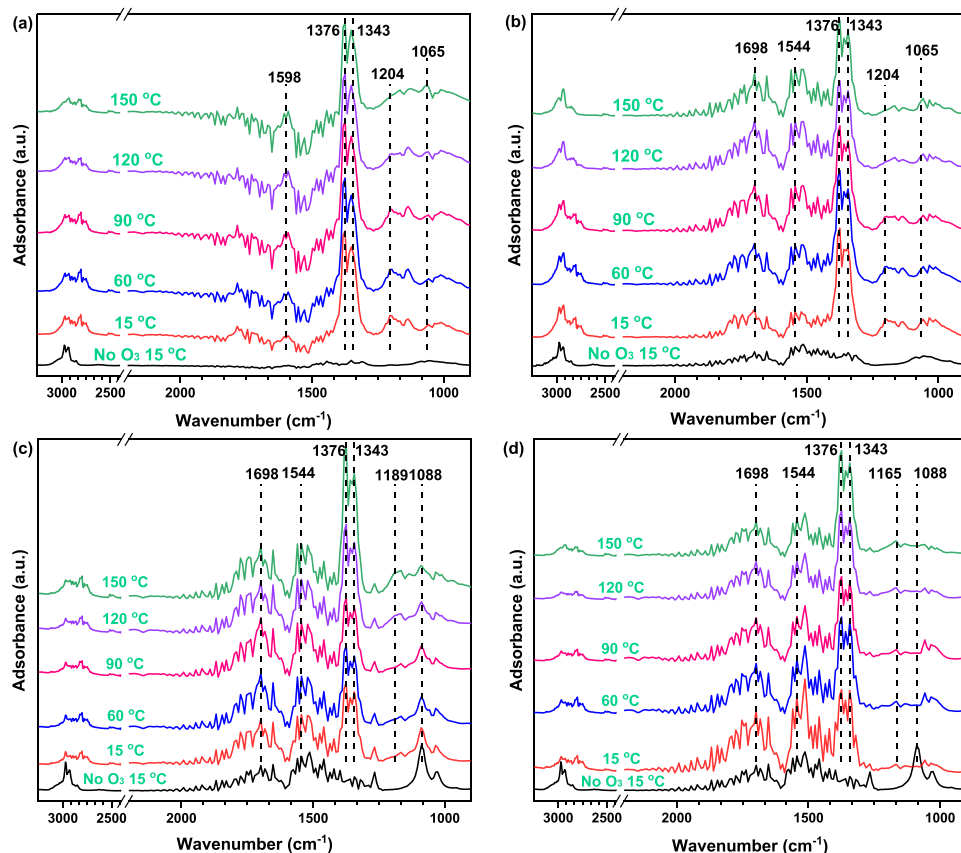


Fig. 6. (a) Gasmet spectra of CH_3SH ozonation at different temperature (total gas flow rate: 500 mL/min); (b) Gasmet spectra of CH_3SH ozonation at different temperature (total gas flow rate: 200 mL/min); (c) Gasmet spectra of CH_3SH catalytic ozonation over Mn@ZSM293 at different temperature; (d) Gasmet spectra of CH_3SH catalytic ozonation over Mn/ZSM293 at different temperature. Initial CH_3SH concentration: 200 ppm, $\text{O}_3/\text{CH}_3\text{SH}:0.7$, 5 vol% O_2 , total gas flow rate: 500 mL/min, catalyst dosage: 0.025 g.

GCMS. In conclusion, catalytic ozonation of CH_3SH can be inferred to involve two steps, i.e., (1) CH_3S^- is oxidized to CH_3SO_3^- , (2) CH_3SO_3^- is further oxidized to SO_4^{2-} , HCOO^- , and SO_2 .

Fig. 7(a)~(b) presents the schematic illustration of Mn@ZSM293 and Mn/ZSM293. Mn nanoparticles are dispersed and confined on the popcorn-like ZSM293 carrier, which is convenient for exposing the active site and binding CH_3SH for reaction. Mn nanoparticles aggregate

into clusters, masking the effective reactive sites and reducing oxygen vacancies. Meanwhile, prismatic ZSM293 is not conducive to the reaction. Fig. 7(c) presents the mechanism for catalytic ozonation of CH_3SH over Mn@ZSM293. Firstly, the gaseous CH_3SH molecule is adsorbed on the surface of Mn@ZSM293. Meanwhile, ozone molecules are trapped in the oxygen vacancies of Mn@ZSM293 and activated into reactive oxygen species (O_2^- , O_2^{2-} , and OH) (Eqs. (1)–(3)) [5]. The transformation

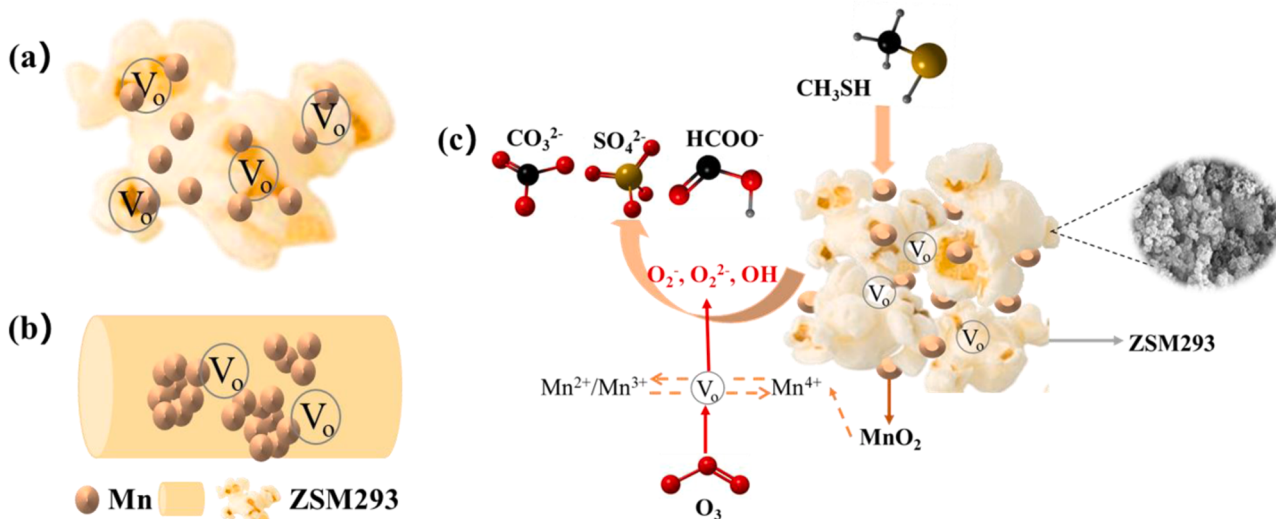
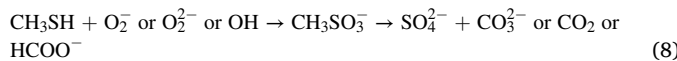
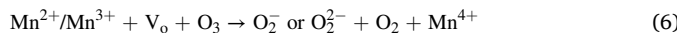


Fig. 7. Schematic illustration of (a) Mn@ZSM293 and (b) Mn/ZSM293. (c) Schematic illustration of CH_3SH catalytic ozonation over Mn@ZSM293.

between MnO_x species with different valence states is accelerated to provide electrons for continuous catalytic ozonation through SMSI, resulting in high apparent activity (Eq. (4)) [12]. Formation of $\text{Mn}^{2+}/\text{Mn}^{3+}$ provides electrons to oxygen vacancies, which are used for ozone activation to generate reactive oxygen species (O_2 or O_2^-). Meanwhile, the transfer of $2\text{O}_{\text{ads}} \rightarrow \text{O}_2$ maintains the electrostatic equilibrium of Mn (Eq. (5)), and Mn^{4+} gets electrons with reduction into $\text{Mn}^{2+}/\text{Mn}^{3+}$. Accordingly, the O_{ads} species $\text{Mn}@\text{ZSM293}$ decreased after the reaction (Table 2). Finally, reactive oxygen species O_2^- , O_2^{2-} , and OH decompose adjacent chemisorbed CH_3SH into intermediate product CH_3SO_3^- , which is further oxidized to SO_4^{2-} , and CO_3^{2-} or CO_2 or HCOO^- (Eq. (6)) [55]. Particularly, $\text{Mn}@\text{ZSM293}$ possesses confined structures similar to popcorn that exhibits abundant structural defects and provides SMSI between MnO_x and ZSM293, which generates more oxygen vacancies to maintain long-term removal efficiency. Ozone assistance further promotes oxidation cycle by formation of superoxide radicals and accelerates the electrons transfer during reaction.



4. Conclusion

This paper reported a popcorn-like catalyst with Mn nanoparticles encapsulated in zeolite ($\text{Mn}@\text{ZSM293}$) for efficient catalytic ozonation of CH_3SH at low temperature. CH_3SH attained 100% conversion at 15 °C with the $\text{O}_3/\text{CH}_3\text{SH}$ molar ratio of 1.33 over $\text{Mn}@\text{ZSM293}$. Particularly, $\text{Mn}@\text{ZSM293}$ exhibited excellent stability without sulfur poisoning, while $\text{Mn}/\text{ZSM293}$ synthesized by conventional impregnated method suffered deactivation. CH_3SH conversion increased with elevation of temperature, and catalytic ozonation mainly had superiority at low temperature compared with homogeneous ozonation. Water presence caused poisoning to some extent, which decreased CH_3SH conversion from 100% to 70% with presence of 10 vol% H_2O at 15 °C. However, water presence promoted CH_3SH conversion at 50 and 75 °C. The excellent stability of $\text{Mn}@\text{ZSM293}$ should attribute to its specific confined structure and strong metal-support interaction (SMSI). SEM images validated that $\text{Mn}@\text{ZSM293}$ possessed the structures with well-defined large internal voids and surface etchings, which could capture gaseous reactants and extend the retention time of the reactants. Especially, several characterizations such as Raman spectra, H₂-TPR, and XPS spectra displayed more oxygen vacancies and higher oxygen mobility of $\text{Mn}@\text{ZSM293}$ compared with $\text{Mn}/\text{ZSM293}$, implying SMSI of $\text{Mn}@\text{ZSM293}$, which further promoted electron transfer during catalytic ozonation. Besides, $\text{Mn}@\text{ZSM293}$ exhibited larger surface area and pore size, as well as abundant Lewis and Brønsted acidic sites, which were favorable for CH_3SH adsorption, activation and breakage of C–C and C–S bonds. All these properties contributed to its excellent catalytic behaviors. Most importantly, the outlet gas was in-situ measured by Gasmet analyzer to obtain the infrared spectra. CH_3S^- , CH_3SO_3^- , SO_4^{2-} , and HCOO^- based compounds were detected as the critical products. Above all, $\text{Mn}@\text{ZSM293}$ with confined structure was confirmed to exhibit strong metal-support interaction that optimized surface properties for catalytic ozonation of CH_3SH at such low temperature.

Catalytic ozonation of S-VOCs provides feasible method for cleaning of sulfur-containing waste gas in chemical production, pharmaceutical

production, sewage treatment and landfill, which is advantaged in low temperature, good stability, and easy operation. Especially, ozone input for S-VOCs is much lower than other VOCs, implying less operation cost. For practical industrial applications, water resistance at lower temperature, optimizing operation parameters to attain the best performance with the lowest input, complete mineralization into CO_2 and soluble sulfur compounds, and ozone leakage should be considered in the future.

CRediT authorship contribution statement

Fawei Lin: Writing – review & editing, Supervision, Funding acquisition, Conceptualization, Formal analysis, Writing – original draft. **Yongtao Li:** Formal analysis, Data curation. **Hang Du:** Methodology, Investigation. **Luyang Zhang:** Writing – original draft, Investigation, Formal analysis, Visualization. **Beibei Yan:** Project administration, Resources. **Zhanjun Cheng:** Methodology, Software, Resources, Writing – review & editing. **Guanyi Chen:** Visualization, Supervision, Resources, Project administration, Writing – review & editing.

Declaration of Competing Interest

The authors declare that they have no known competing financial interests or personal relationships that could have appeared to influence the work reported in this paper

Data availability

Data will be made available on request.

Acknowledgments

This work is supported by the National Natural Science Foundation of China (52376205).

Appendix A. Supporting information

Supplementary data associated with this article can be found in the online version at doi:10.1016/j.apcatb.2024.123908.

References

- [1] Y.-H. Lin, T.-K. Tseng, H. Chu, Photo-catalytic degradation of dimethyl disulfide on S and metal-ions co-doped TiO₂ under visible-light irradiation, *Appl. Catal. A-Gen.* 469 (2014) 221–228.
- [2] J. Yang, Q. Zhang, F. Zhang, D. Xia, H. Liu, S. Tian, L. Sun, D. Shu, C. He, S. Runa, Three-dimensional hierarchical porous sludge-derived carbon supported on silicon carbide foams as effective and stable Fenton-like catalyst for odorous methyl mercaptan elimination, *J. Hazard. Mater.* 358 (2018) 136–144.
- [3] W. Qu, Z. Tang, W. Liu, Y. Liao, Y. Huang, D. Xia, Q. Lian, S. Tian, C. He, D. Shu, Self-accelerating interfacial catalytic elimination of gaseous sulfur-containing volatile organic compounds as microbubbles in a facet-engineered three-dimensional BiOCl Sponge Fenton-like Process, *Environ. Sci. Technol.* (2022).
- [4] J.P. Liu, H. Su, Y.A. Hu, C.H. Gong, J.C. Lu, D.D. He, W.J. Zhu, D.K. Chen, X.H. Cao, J. Li, S. Gligorovski, Y.M. Luo, Highly efficient degradation of sulfur-containing volatile organic compounds by amorphous MnO₂ at room temperature: implications for controlling odor pollutants, *Appl. Catal., B* 334 (2023) 122877.
- [5] J. Yang, Y. Huang, Y.-W. Chen, D. Xia, C.-Y. Mou, L. Hu, J. Zeng, C. He, P.K. Wong, H.-Y. Zhu, Active site-directed tandem catalysis on CuO/VO-MnO₂ for efficient and stable catalytic ozonation of S-VOCs under mild condition, *Nano Today* 35 (2020) 100944.
- [6] H. Su, J. Liu, Y. Hu, T. Ai, C. Gong, J. Lu, Y. Luo, Comparative Study of alpha- and beta-MnO₂ on methyl mercaptan decomposition: the role of oxygen vacancies, *Nanomaterials* 13 (2023).
- [7] X.L. Weng, Y. Long, W.L. Wang, M. Shao, Z.B. Wu, Structural effect and reaction mechanism of MnO₂ catalysts in the catalytic oxidation of chlorinated aromatics, *Chinese J. Catal.* 40 (2019) 638–646.
- [8] X.H. Cao, T.H. Ai, Z.Z. Xu, J.C. Lu, D.K. Chen, D.D. He, J.P. Liu, R. Tian, Y.T. Zhao, Y.M. Luo, Insights into the different catalytic behavior between Ce and Cr modified MCM-41 catalysts: Cr₂S₃ as new active species for CH₃SH decomposition, *Sep. Purif. Technol.* 307 (2023) 122742.
- [9] J.C. Lu, R. Tian, W.J. Zhang, Y.L. Zhang, Y.J. Yang, Z.Z. Xu, D.D. He, T.H. Ai, Y. M. Luo, An ultra-long stability of lanthanum (La) modified molecular sieve for

catalytic degradation of typical sulfur-containing VOCs in a near-real environment, *Appl. Catal. B* 339 (2023) 123114.

[10] Y.T. Zhao, D.K. Chen, J.P. Liu, D.D. He, X.H. Cao, C.Y. Han, J.C. Lu, Y.M. Luo, Tuning the metal-support interaction on chromium-based catalysts for catalytically eliminate methyl mercaptan: anchored active chromium species through surface hydroxyl groups, *Chem. Eng. J.* 389 (2020) 124384.

[11] R. Tian, J.C. Lu, Z.Z. Xu, W.J. Zhang, J.P. Liu, L.L. Wang, Y.B. Xie, Y.T. Zhao, X. H. Cao, Y.M. Luo, Unraveling the synergistic reaction and the deactivation mechanism for the catalytic degradation of double components of sulfur-containing VOCs over ZSM-5-based materials, *Environ. Sci. Technol.* 57 (2023) 1443–1455.

[12] D. Xia, W. Xu, Y. Wang, J. Yang, Y. Huang, L. Hu, C. He, D. Shu, D.Y.C. Leung, Z. Pang, Enhanced performance and conversion pathway for catalytic ozonation of methyl mercaptan on single-atom Ag deposited three-dimensional ordered mesoporous MnO₂, *Environ. Sci. Technol.* 52 (2018) 13399–13409.

[13] C. He, Y.H. Liao, C. Chen, D.H. Xia, Y.Y. Wang, S.H. Tian, J.L. Yang, D. Shu, Realizing a redox-robust Ag/MnO₂ catalyst for efficient wet catalytic ozonation of S-VOCs: Promotional role of Ag(0)/Ag(I)-Mn based redox shuttle, *Appl. Catal. B-Environ.* 303 (2022) 11.

[14] J. Yang, Y. Huang, Y.-W. Chen, D. Xia, C.-Y. Mou, L. Hu, J. Zeng, C. He, P.K. Wong, H.-Y. Zhu, Active site-directed tandem catalysis on CuO/V-O-MnO₂ for efficient and stable catalytic ozonation of S-VOCs under mild condition, *Nano Today* 35 (2020).

[15] Y. Zhao, D. Chen, J. Liu, D. He, X. Cao, C. Han, J. Lu, Y. Luo, Tuning the metal-support interaction on chromium-based catalysts for catalytically eliminate methyl mercaptan: Anchored active chromium species through surface hydroxyl groups, *Chem. Eng. J.* 389 (2020).

[16] L. Yang, Q. Liu, R. Han, K. Fu, Y. Su, Y. Zheng, X. Wu, C. Song, N. Ji, X. Lu, D. Ma, Confinement and synergy effect of bimetallic Pt-Mn nanoparticles encapsulated in ZSM-5 zeolite with superior performance for acetone catalytic oxidation, *Appl. Catal. B-Environ.* 309 (2022).

[17] R.M. Fang, H.B. Huang, W.J. Huang, J. Ji, Q.Y. Feng, Y.J. Shu, Y.J. Zhan, G.Y. Liu, R.J. Xie, Influence of peracetic acid modification on the physicochemical properties of activated carbon and its performance in the ozone-catalytic oxidation of gaseous benzene, *Appl. Surf. Sci.* 420 (2017) 905–910.

[18] C. Ramakrishna, S.C. Shekar, A.K. Gupta, B. Saini, R. Krishna, G. Sreetha, T. Gopi, Degradation of diethyl sulfide vapors with manganese oxide catalysts supported on zeolite-13X: the influence of process parameters and mechanism in presence of ozone, *J. Environ. Chem. Eng.* 5 (2017) 1484–1493.

[19] W. Qu, Z.Y. Tang, H.L. Wen, M.H. Luo, T. Zhong, Q.Y. Lian, L.L. Hu, S.H. Tian, C. He, D. Shu, Electron Transfer Trade-offs in MOF-Derived Cobalt-Embedded Nitrogen-Doped Carbon Nanotubes Boost Catalytic Ozonation for Gaseous Sulfur-Containing VOC Elimination, *ACS Catal.* 13 (2023) 692–705.

[20] W. Qu, Z.Y. Tang, W. Liu, Y.H. Liao, Y.J. Huang, D.H. Xia, Q.Y. Lian, S.H. Tian, C. He, D. Shu, Self-accelerating interfacial catalytic elimination of gaseous sulfur-containing volatile organic compounds as microbubbles in a facet-engineered three-dimensional BiOCl sponge fenton-like process, *Environ. Sci. Technol.* (2022) 11657–11669.

[21] Y. Wu, C. Ye, L. Yu, Y. Liu, J. Huang, J. Bi, L. Xue, J. Sun, J. Yang, W. Zhang, X. Wang, P. Xiong, J. Zhu, Soft template-directed interlayer confinement synthesis of a Fe-Co dual single-atom catalyst for Zn-air batteries, *Energy Storage Mater.* 45 (2022) 805–813.

[22] X. Wu, R. Han, Q. Liu, Y. Su, S. Lu, L. Yang, C. Song, N. Ji, D. Ma, X. Lu, A review of confined-structure catalysts in the catalytic oxidation of VOCs: synthesis, characterization, and applications, *Catal. Sci. Technol.* 11 (2021) 5374–5387.

[23] Z. Jiang, W. Zhou, C. Hu, X. Luo, W. Zeng, X. Gong, Y. Yang, T. Yu, W. Lei, C. Yuan, Interlayer-confined NiFe₂ dual atoms within MoS₂ electrocatalyst for ultra-efficient acidic overall water splitting, *Adv. Mater.* 35 (2023).

[24] G.X. Zhu, W. Zhu, Y. Lou, J. Ma, W.Q. Yao, R.L. Zong, Y.F. Zhu, Encapsulate alpha-MnO₂ nanofiber within graphene layer to tune surface electronic structure for efficient ozone decomposition, *Nat. Commun.* 12 (2021) 10.

[25] E. Wu, X. Feng, Y. Zheng, D. Lin, Y. Luo, Y. You, B. Huang, Q. Qian, Q. Chen, Inverse coprecipitation directed porous core-shell Mn-Co-O catalyst for efficient low temperature propane oxidation, *ACS Sustain. Chem. Eng.* 8 (2020) 5787–5798.

[26] J. Shao, Y. Zhai, L. Zhang, L. Xiang, F. Lin, Low-Temperature catalytic ozonation of multitype VOCs over zeolite-supported catalysts, *Int. J. Environ. Res. Public Health* 19 (2022).

[27] G.Y. Chen, Z. Wang, F.W. Lin, Z.M. Zhang, H.D. Yu, B.B. Yan, Z.H. Wang, Comparative investigation on catalytic ozonation of VOCs in different types over supported MnO_x catalysts, *J. Hazard. Mater.* 391 (2020) 17.

[28] Z. Zhang, L. Xiang, F. Lin, Z. Wang, B. Yan, G. Chen, Catalytic deep degradation of Cl-VOCs with the assistance of ozone at low temperature over MnO₂ catalysts, *Chem. Eng. J.* 426 (2021) 130814.

[29] F. Lin, Z. Zhang, L. Xiang, L. Zhang, Z. Cheng, Z. Wang, B. Yan, G. Chen, Efficient degradation of multiple Cl-VOCs by catalytic ozonation over MnO_x catalysts with different supports, *Chem. Eng. J.* 435 (2022) 134807.

[30] G. Bae, H. Kim, H. Choi, P. Jeong, D.H. Kim, H.C. Kwon, K.-S. Lee, M. Choi, H.-S. Oh, F. Jaouen, C.H. Choi, Quantification of active site density and turnover frequency: from single-atom metal to nanoparticle electrocatalysts, *Jacs Au* 1 (2021) 586–597.

[31] Y. Zhang, J. Lu, L. Zhang, T. Fu, J. Zhang, X. Zhu, X. Gao, D. He, Y. Luo, D. Dionysiou, W. Zhu, Investigation into the catalytic roles of oxygen vacancies during gaseous styrene degradation process via CeO₂ catalysts with four different morphologies, *Appl. Catal. B-Environ.* 309 (2022).

[32] Z.H. Xu, W.H. Yang, W.Z. Si, J.J. Chen, Y. Peng, J.H. Li, A novel gamma-like MnO₂ catalyst for ozone decomposition in high humidity conditions, *J. Hazard. Mater.* 420 (2021).

[33] P. Wang, J. Wang, X. An, J. Shi, W. Shangguan, X. Hao, G. Xu, B. Tang, A. Abudula, G. Guan, Generation of abundant defects in Mn-Co mixed oxides by a facile agar-gel method for highly efficient catalysis of total toluene oxidation, *Appl. Catal. B-Environ.* 282 (2021).

[34] M. Aghbolagh, M. Ghavami, J. Soltan, N. Chen, Effect of active metal loading on catalyst structure and performance in room temperature oxidation of acetone by ozone, *J. Ind. Eng. Chem.* 77 (2019) 118–127.

[35] S.Y. Gong, W.H. Li, Z. Xie, X. Ma, H.D. Liu, N. Han, Y.F. Chen, Low temperature decomposition of ozone by facilely synthesized cuprous oxide catalyst, *N. J. Chem.* 41 (2017) 4828–4834.

[36] Z.H. Xu, W.H. Yang, W.Z. Si, J.J. Chen, Y. Peng, J.H. Li, A novel gamma-like MnO₂ catalyst for ozone decomposition in high humidity conditions, *J. Hazard. Mater.* 420 (2021) 13.

[37] L. Xiang, F. Lin, B. Cai, G. Li, L. Zhang, Z. Wang, B. Yan, Y. Wang, G. Chen, Catalytic ozonation of CH₂Cl₂ over hollow urchin-like MnO₂ with regulation of active oxygen by catalyst modification and ozone promotion, *J. Hazard. Mater.* 436 (2022).

[38] Z.Y. Xu, S.P. Mo, Y.X. Li, Y.C. Zhang, J.L. Wu, M.L. Fu, X.J. Niu, Y. Hu, D.Q. Ye, Pt/MnO_x for toluene mineralization via ozonation catalysis at low temperature: SMSI optimization of surface oxygen species, *Chemosphere* 286 (2022) 10.

[39] J. Ding, J. Chen, Z. Rui, Y. Liu, P. Lv, X. Liu, H. Li, H. Ji, Synchronous pore structure and surface hydroxyl groups amelioration as an efficient route for promoting HCHO oxidation over Pt/ZSM-5, *Catal. Today* 316 (2018) 107–113.

[40] L.L. Yu, M.F. Khan, G. Achari, A review on physicochemical treatment of sulfolane in aqueous media, *J. Environ. Chem. Eng.* 9 (2021) 11.

[41] K.C. Soni, S.C. Shekar, B. Singh, T. Gopi, Catalytic activity of Fe/ZrO₂ nanoparticles for dimethyl sulfide oxidation, *J. Colloid Interface Sci.* 446 (2015) 226–236.

[42] S. Rong, P. Zhang, F. Liu, Y. Yang, Engineering crystal facet of alpha-MnO₂ nanowire for highly efficient catalytic oxidation of carcinogenic airborne formaldehyde, *ACS Catal.* 8 (2018) 3435–3446.

[43] W.-Z. Yu, X.-P. Fu, K. Xu, C. Ling, W.-W. Wang, C.-J. Jia, CO₂ methanation catalyzed by a Fe-Co/Al2O3 catalyst, *J. Environ. Chem. Eng.* 9 (2021).

[44] J.M. Shao, F.W. Lin, Z.H. Wang, P.X. Liu, H.R. Tang, Y. He, K.F. Cen, Low temperature catalytic ozonation of toluene in flue gas over Mn-based catalysts: effect of support property and SO₂/water vapor addition, *Appl. Catal. B-Environ.* 266 (2020) 11.

[45] J. Kim, E.E. Kwon, J.E. Lee, S.-H. Jang, J.-K. Jeon, J. Song, Y.-K. Park, Effect of zeolite acidity and structure on ozone oxidation of toluene using Ru-Mn loaded zeolites at ambient temperature, *J. Hazard. Mater.* 403 (2021).

[46] J. Bing, Y. Xu, C. Wu, X. Lv, X. Xiao, L. Chen, Mechanism of catalytic ozonation in different surface acid sites of oxide aqueous suspensions, *Environ. Sci. -Nano* 10 (2023) 2312–2323.

[47] Y. Chen, W. Qu, T. Luo, H. Zhang, J. Fu, H. Li, C. Liu, D. Zhang, M. Liu, Promoting C-F bond activation via proton donor for CF₄ decomposition, *Proc. Natl. Acad. Sci. U. S. A.* 120 (2023) e2312480120–e2312480120.

[48] F. Lin, Z. Zhang, N. Li, B. Yan, C. He, Z. Hao, G. Chen, How to achieve complete elimination of Cl-VOCs: a critical review on byproducts formation and inhibition strategies during catalytic oxidation, *Chem. Eng. J.* 404 (2021) 126534.

[49] F.W. Lin, Z.H. Wang, Q. Ma, Y. Yang, R. Whiddon, Y.Q. Zhu, K.F. Cen, Catalytic deep oxidation of NO by ozone over MnO_x loaded spherical alumina catalyst, *Appl. Catal. B-Environ.* 198 (2016) 100–111.

[50] Y. Yuan, K. He, B.W. Byles, C. Liu, K. Amine, J. Lu, E. Pomerantseva, R. Shahbazian-Yassar, Deciphering the atomic patterns leading to MnO₂ polymorphism, *Chem* 5 (2019) 1793–1805.

[51] R.X. Zhao, D.D. Jin, H.S. Yang, S.Y. Lu, P.M. Potter, C.C. Du, Y.Q. Peng, X.D. Li, J. H. Yan, Low-temperature catalytic decomposition of 130 tetra- to octa-PCDD/Fs Congeners over CuOx and MnO_x modified V2O5/TiO₂-CNTs with the assistance of O-3, *Environ. Sci. Technol.* 50 (2016) 11424–11432.

[52] Z. Xiong, L. Lan, Y. Wang, C. Lu, S. Qin, S. Chen, L. Zhou, C. Zhu, S. Li, L. Meng, K. Sun, Y. Li, Multifunctional polymer framework modified SnO₂ enabling a photostable α -FAPbI₃ perovskite solar cell with efficiency exceeding 23%, *Acc. Energy Lett.* 6 (2021) 3824–3830.

[53] M.Z. Tian, S.J. Liu, L.L. Wang, H. Ding, D. Zhao, Y.Q. Wang, J.H. Cui, J.F. Fu, J. Shang, G.K. Li, Complete degradation of gaseous methanol over Pt/FeO_x catalysts by normal temperature catalytic ozonation, *Environ. Sci. Technol.* 54 (2020) 1938–1945.

[54] F. Lin, Z. Wang, Z. Zhang, L. Xiang, D. Yuan, B. Yan, Z. Wang, G. Chen, Comparative investigation on chlorobenzene oxidation by oxygen and ozone over a MnO_x/Al2O3 catalyst in the presence of SO₂, *Environ. Sci. Technol.* 55 (2021) 3341–3351.

[55] C. He, Y. Wang, Z. Li, Y. Huang, Y. Liao, D. Xia, S. Lee, Facet engineered alpha-MnO₂ for efficient catalytic ozonation of odor CH₃SH: oxygen vacancy-induced active centers and catalytic mechanism, *Environ. Sci. Technol.* 54 (2020) 12771–12783.